

Zeeman and laser site selective spectroscopy of C_1 point group symmetry Sm^{3+} centers in Y_2SiO_5 : a parametrized crystal-field analysis for the $4f^5$ configuration

N. L. Jobbitt,^{1,2} J.-P. R. Wells,^{1,2,*} and M. F. Reid^{1,2,†}

¹*School of Physical and Chemical Sciences, University of Canterbury, PB4800 Christchurch 8140, New Zealand*

²*The Dodd-Walls Centre for Photonic and Quantum Technologies, New Zealand*

(Dated: June 23, 2022)

Parametrized crystal-field analyses are presented for both the six and seven fold coordinated, C_1 symmetry Sm^{3+} centers in Y_2SiO_5 , based on extensive spectroscopic data spanning the infrared to optical regions. Laser site-selective excitation and fluorescence spectroscopy as well as Zeeman absorption spectroscopy performed along multiple crystallographic directions has been utilised, in addition to previously determined g tensors for the ${}^6H_{5/2}Z_1$ and ${}^4G_{5/2}A_1$ states. The resultant analyses give good approximation to the experimental energy levels and magnetic splittings, yielding crystal-field parameters consistent with the few other lanthanide ions for which such analyses are available.

Keywords: Zeeman spectroscopy, laser site selective spectroscopy, low symmetry crystal-field analysis

I. INTRODUCTION

Rare-earth doped Y_2SiO_5 is an attractive option for the development of quantum storage and communication devices due to the low nuclear spin of yttrium ($I = 1/2$) and the low abundances of silicon and oxygen isotopes with non-zero nuclear spins [1, 2]. Thus the effects of nuclear spin-flips on neighbouring ions on the decoherence times of lanthanide ions doped into this materials system are minimized, resulting in observed hyperfine coherence times exceeding 1 minute for $Pr^{3+}:Y_2SiO_5$ and 6 hours in the case of $Eu^{3+}:Y_2SiO_5$ [3, 4]. Y_2SiO_5 has therefore been the focus of many studies, providing demonstrations of quantum memories [2, 4–7], quantum gate implementations [8, 9], and single photon sources [10]. Recently, demonstrations have been made showing control of multiple ions at the single-photon level [11].

The key technique utilized in obtaining such long coherence times is the zero-first-order Zeeman (ZEFOZ) technique, which involves determining magnetic field points for which the magnetic-hyperfine structure is insensitive to magnetic field fluctuations in any direction. However, ZEFOZ points are notoriously difficult to find experimentally and would optimally be predicted through a crystal-field calculation. Such an approach has the additional benefit of being able to predict the electronic and magnetic-hyperfine structure of the entire $4f^N$ configuration of lanthanide doped Y_2SiO_5 , whereas more conventional approaches, such as the utilization of a spin Hamiltonian, are only able to predict the magnetic-hyperfine structure of a single state. Previously determined spin Hamiltonian parameters were necessary in

obtaining the observed coherence times for $Pr^{3+}:Y_2SiO_5$ and $Eu^{3+}:Y_2SiO_5$ [3, 4, 12–14].

Y_2SiO_5 doped with Kramers ions, such as Sm^{3+} and Er^{3+} , are appealing candidates in the realization of high-bandwidth quantum storage and communication devices, due to the large hyperfine splittings of such ions, whilst still retaining reasonably long coherence times. $Er^{3+}:Y_2SiO_5$ has been observed to have a hyperfine coherence time of 1.3 s at high magnetic field strengths [7], while hyperfine coherence times of 1 ms for $Yb^{3+}:Y_2SiO_5$ and 1.48 ms for $Er^{3+}:Y_2SiO_5$ have been observed without the need of an external magnetic field [15, 16]. These studies utilized previously determined spin Hamiltonian parameters in order to obtain the observed coherence times [17, 18]. $Sm^{3+}:Y_2SiO_5$ serves as a alternative in the realization of high-bandwidth quantum storage and communication devices, due to the small ground state g values, which results in an intrinsic insensitivity to magnetic field fluctuations [19]. Furthermore, the 15% natural abundance of both isotopes with a non-zero nuclear spin ($I = 7/2$ for either ${}^{147}Sm$ or ${}^{149}Sm$), allows for the possibility of many ZEFOZ points within the complex magnetic-hyperfine structure of $Sm^{3+}:Y_2SiO_5$, from which, a single ZEFOZ transition belonging to either isotope could be utilized in the development of high-bandwidth quantum storage and communication devices.

Crystal-field analyses for C_1 point group symmetry sites, such as those of Y_2SiO_5 , are difficult to perform as extensive data including orientational information, such as magnetic g values for multiple crystallographic directions, can be required in order to obtain a unique, global fit. Currently, crystal-field analyses have been reported for Ce^{3+} , Er^{3+} and Yb^{3+} doped Y_2SiO_5 [20–23], with further modelling in progress for other ions [24, 25].

In this work, we present a parameterized crystal-field analysis for both crystallographic sites of Sm^{3+} doped into Y_2SiO_5 , which accurately reproduces the electronic and magnetic structure up to the ${}^4G_{7/2}$ multiplet at $\sim 20000\text{ cm}^{-1}$. Laser site-selective excitation and fluorescence, coupled with Zeeman absorption spectroscopy has been performed in order to obtain the data required. Ap-

* jon-paul.wells@canterbury.ac.nz

† mike.reid@canterbury.ac.nz

proximately fifty-five electronic energy levels and eighty g values, obtained along all three crystallographic axes, in addition to magnetic splittings determined from the previously determined g tensors of the ${}^6\text{H}_{5/2}\text{Z}_1$ and ${}^4\text{G}_{5/2}\text{A}_1$ states [19], were fitted simultaneously for each site in order to uniquely determine the 32 free parameters used in the crystal-field fit. The ground state hyperfine structure has been predicted using the wavefunctions obtained from the crystal-field calculation with similar splittings to what has been reported for $\text{Er}^{3+}:\text{Y}_2\text{SiO}_5$ predicted, and significantly larger than what has been observed for $\text{Eu}^{3+}:\text{Y}_2\text{SiO}_5$ [14, 21]. This, together with the low ground state g -values, suggest $\text{Sm}^{3+}:\text{Y}_2\text{SiO}_5$ could be a previously overlooked material for the development of high-bandwidth quantum information storage and communications devices.

II. EXPERIMENTAL

Y_2SiO_5 has a monoclinic crystal structure with C_{2h}^{6h} space group symmetry. The lattice constants of Y_2SiO_5 are; $a = 10.4103 \text{ \AA}$, $b = 6.7212 \text{ \AA}$, $c = 12.4905 \text{ \AA}$, and $\beta = 102^\circ 39'$ [26]. The C_2 rotation axis corresponds to the b axis, while the a and c axes are located in the plane perpendicular to the b axis. Here we follow the conventions used in [27], by defining the optical extinction axes D_1 and D_2 , which are located in the a - c plane and are perpendicular to each other in addition to the b axis. In this study we focus on the X_2 phase of Y_2SiO_5 , which has two C_1 symmetry sites, labelled as site 1 and site 2, having coordination numbers of six and seven respectively. Each site possesses two magnetically inequivalent orientations that are related by a 180° rotation about the b axis. These two orientations respond differently when a magnetic field is applied outside of the b axis or the D_1 - D_2 plane [28].

The sample used in this study was grown in the X_2 phase of Y_2SiO_5 via the Czochralski method by Scientific Materials Inc. (Bozeman, USA). The sample was grown with a samarium dopant concentration of 0.5 molar % and was cut to have dimensions of $(5.1 \pm 0.1) \text{ mm}$ along the D_1 axis, $(4.9 \pm 0.1) \text{ mm}$ along the D_2 axis, and $(6.0 \pm 0.2) \text{ mm}$ along the crystallographic b axis.

Laser site-selective excitation and fluorescence spectroscopy was performed using a PTI GL-302 tunable dye laser, which was pumped using a PTI GL-3300 pulsed nitrogen laser. The sample fluorescence was monitored by a Horiba iHR550 spectrometer coupled with either an air cooled Hamamatsu H10330C near infrared photomultiplier tube or a water-cooled Hamamatsu C9727 visible photomultiplier tube connected to appropriate photon counting units. The sample was cooled to 10 K using a Janis CCS-150 closed cycle cryostat coupled to a Lakeshore 325 temperature controller via a resistive heater attached to the back of the sample cold finger.

Zeeman absorption spectroscopy was performed using a Bruker Vertex-80 Fourier transform infrared (FTIR)

spectrometer providing a maximum apodized resolution of 0.075 cm^{-1} and having a spectral range of 700-30,000 cm^{-1} , with the entire beam path purged by dry N_2 gas to minimise atmospheric water. The sample was mounted into the bore of a 4 Tesla simple solenoid and cooled to 4.2 K via thermal contact with the cryostat's liquid helium bath.

III. RESULTS AND DISCUSSION

The $4f^5$ configuration, appropriate to trivalent samarium, consists of 1001 two fold degenerate Kramers states. In this work, we adopt the standard notation of a letter plus a numerical subscript to label the crystal-field levels of the LSJ multiplets. These follow the convention utilised in the standard 'Dieke diagram'.

A. Laser site selective spectroscopy

Figure 1 shows the 10 K fluorescence spectra for both Sm^{3+} sites in Y_2SiO_5 for transitions to all multiplets of the ${}^6\text{H}$ and ${}^6\text{F}$ terms. All fluorescence is observed to emanate from the ${}^4\text{G}_{5/2}$ multiplet regardless of the exact excitation wavelength. To obtain fluorescence to the ${}^6\text{H}_{5/2}$ multiplet, the ${}^6\text{H}_{5/2}\text{Z}_1 \rightarrow {}^4\text{F}_{3/2}\text{B}_1$ transition at 18 913 cm^{-1} for site 1 and 18 955 cm^{-1} for site 2 was optically pumped. For all other multiplets, the ${}^6\text{H}_{5/2}\text{Z}_1 \rightarrow {}^4\text{G}_{5/2}\text{A}_1$ transition at 17 689 cm^{-1} for site 1 and 17 790 cm^{-1} for site 2 was excited. Assignments were confirmed using 10 K absorption spectroscopy.

Figure 2 shows 10 K broadband and site-selective excitation spectra for the ${}^4\text{G}_{5/2}$, ${}^4\text{F}_{3/2}$ and ${}^4\text{G}_{7/2}$ multiplets of both sites in $\text{Sm}^{3+}:\text{Y}_2\text{SiO}_5$. The broadband spectra were obtained by monitoring all ${}^4\text{G}_{5/2} \rightarrow {}^6\text{H}_{9/2}$ fluorescence centered on 15 300 cm^{-1} . The ${}^4\text{G}_{5/2}$ site-selective excitation spectra were obtained by monitoring the ${}^4\text{G}_{5/2}\text{A}_1 \rightarrow {}^6\text{H}_{9/2}\text{X}_1$ fluorescence at 15 338 cm^{-1} for site 1 and the ${}^4\text{G}_{5/2}\text{A}_1 \rightarrow {}^6\text{H}_{7/2}\text{Y}_1$ fluorescence at 16 672 cm^{-1} for site 2. Site-selective excitation spectra for the ${}^4\text{F}_{3/2}$ and ${}^4\text{G}_{7/2}$ multiplets were obtained by monitoring the ${}^4\text{G}_{5/2}\text{A}_1 \rightarrow {}^6\text{H}_{5/2}\text{Z}_1$ fluorescence at 17 689 cm^{-1} and 17 790 cm^{-1} for site 1 and site 2 respectively. The spectral features seen in the site 1 fluorescence spectra while exciting the ${}^4\text{G}_{5/2}$ and ${}^4\text{F}_{3/2}$ multiplets are related to site 2 and is due to inter-site energy transfer, as reported previously [29].

A total of 56 electronic energy levels are determined for site 1 and 58 electronic energy levels for site 2 through the use of site-selective excitation and fluorescence spectroscopy. These values are summarized in Tables I and II for site 1 and site 2 respectively.

Phonon sidebands are commonly observed in excitation spectra measured for the $\text{Sm}^{3+} {}^4\text{G}_{5/2}$ multiplet (see for example, refs [30-32]). For Y_2SiO_5 such vibronic structure is also observable as shown in Fig. 2. The

observed phonon sideband structure is observed to be shifted from the $\text{Sm}^{3+} \ ^6\text{H}_{5/2} \rightarrow \ ^4\text{G}_{5/2}$ zero-phonon electronic lines, in the range 100 to 750 cm^{-1} . Comparable structure can be observed in some of the fluorescence spectra Fig. 1. These are consistent with the calculated phonon density of states for Y_2SiO_5 [33].

B. Zeeman absorption spectroscopy

Directional information is required as an input for low symmetry crystal-field analyses in order to obtain a global minimum. Thus the (linear and non-linear) splittings of the Sm^{3+} ion Kramers doublets under the influence of an external magnetic field along multiple crystallographic directions have been measured. Zeeman absorption spectroscopy was performed on all observable transitions between 1500-20000 cm^{-1} , using field up to 4 T in magnitude, in order to obtain the required data. Previously, the g tensors of the $\ ^6\text{H}_{5/2}\text{Z}_1$ and $\ ^4\text{G}_{5/2}\text{A}_1$ states for both sites have been reported [19].

Figures 3 and 4 show representative Zeeman absorption spectra for the $\ ^6\text{H}_{5/2}\text{Z}_1 \rightarrow \ ^6\text{H}_{13/2}\text{V}_1$ transition for site 1 and site 2 respectively, obtained at 4.2 K. The top, middle and bottom panels show the magnetic splittings with a magnetic field applied parallel to the D_1 , D_2 and b axes respectively. The left panels show 4.2 K Zeeman absorption spectra at a magnetic field strength of 4 T. The right panels depict the experimental magnetic splittings, given by the circles, and the theoretical magnetic splittings, given by the red lines. In general, the calculated values give good approximation to the experimental data.

A total of 72 g values (25 along the D_1 axis, 22 along the D_2 axis and 25 along the b axis) for site 1 and 92 g values (34 along the D_1 axis, 28 along the D_2 axis and 30 along the b axis) for site 2 were determined utilizing Zeeman absorption spectroscopy. These g values are summarized in Tables I and II for site 1 and site 2 respectively. Due to the very small ground state g values afforded in $\text{Sm}^{3+}:\text{Y}_2\text{SiO}_5$ [19], most transitions were found to split into two transitions. In these cases, the observed splitting is approximately the excited state value.

C. Parameterized crystal-field analysis

The Hamiltonian used to model the $4f^5$ configuration of $\text{Sm}^{3+}:\text{Y}_2\text{SiO}_5$ can be written as [34]:

$$H = H_{FI} + H_{CF} + H_{HF} + H_Q + H_Z \quad (1)$$

where H_{FI} denotes the free-ion interactions, H_{CF} describes the crystal-field interaction, while H_Z describes the Zeeman interaction. The free-ion Hamiltonian has

an explicit form:

$$\begin{aligned} H_{FI} = & E_{\text{avg}} + \sum_{k=0,2,4,6} F^k f_k + \zeta_{nl} A_{SO}(nl) \\ & + \alpha L(L+1) + \beta G(G_2) + \gamma G(R_7) \\ & + \sum_{i=2,3,4,6,7,8} T^i t_i + \sum_{i=0,2,4} M^i m_i + \sum_{i=2,4,6} P^i p_i \end{aligned} \quad (2)$$

where E_{avg} represents the configuration barycenter, Aspherical electrostatic repulsion is parameterized by the Slater parameters, F_k , while ζ describes the spin-orbit interaction. α , β and γ are the two-body (Trees) parameters, while T_i are the three-body (Judd) parameters. Finally higher order effects, such as spin-spin and spin-other-orbit in addition to electrostatically correlated magnetic interactions are described by the M^i and P^i parameters respectively. Here we constrained the M^i and P^i parameters to the ratios determined by [35].

The crystal-field Hamiltonian is commonly written as:

$$H_{CF} = \sum_{k,q} B_q^k C_q^{(k)} \quad (3)$$

where the B_q^k are the coefficients of the expansion of the crystal-field (the crystal-field parameters) in terms of the $C_q^{(k)}$ - the Racah spherical tensors, expressed in Wybourne's normalization. In the C_1 point group symmetry substitutional sites available in the Y_2SiO_5 host crystal, $k = 2, 4, 6$ and $q = -k, \dots, k$. All non-axial ($q \neq 0$) parameters are complex, leading to a total of 27 independent parameters to be determined.

H_{HF} and H_Q are the contributions from magnetic dipole and electric quadrupole moment interactions respectively.

The contribution due to the magnetic dipole is given as [36]:

$$H_{HF} = a_l \sum_i \mathbf{N}_i \cdot \mathbf{I} \quad (4)$$

where,

$$\mathbf{N}_i = \mathbf{l}_i - \sqrt{10} (s\mathbf{C}^{(2)})_i^{(1)} \quad (5)$$

here \mathbf{l}_i and \mathbf{s}_i are the orbital and spin angular momenta of the i^{th} electron respectively, while \mathbf{I} is the nuclear spin operator. The magnetic dipole hyperfine parameter, a_l , is given as [37]:

$$a_l = 2\mu_B g_n \mu_N \frac{\mu_0}{4\pi} (1-R) \langle r_e^{-3} \rangle \quad (6)$$

where μ_B and μ_N are the Bohr magneton and nuclear magneton respectively, μ_0 is the vacuum permeability, R is a shielding factor describing the effect of the induced closed shell quadrupole moment on the 4f electrons, and $\langle r_e^{-3} \rangle$ is the average inverse-cube radius of the 4f orbital.

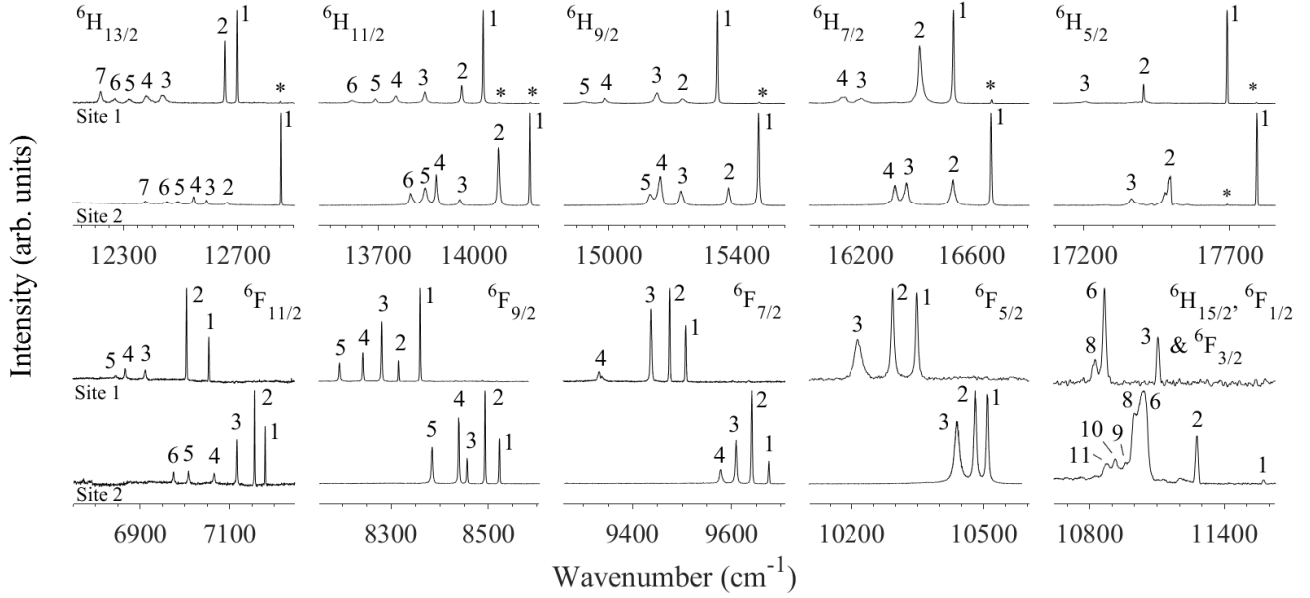


FIG. 1. 10 K site-selective fluorescence spectra of site 1 (top spectra in each panel) and site 2 (bottom spectra in each panel) in $\text{Sm}^{3+}:\text{Y}_2\text{SiO}_5$. Numbered peaks are assigned to their respective site. Spectral features marked with an ‘*’ are transitions related to the other site. The additional structure observable in the spectra for the ${}^6\text{H}_{5/2}$, ${}^6\text{H}_{13/2}$, ${}^6\text{H}_{15/2}$, ${}^6\text{F}_{1/2}$ and ${}^6\text{F}_{3/2}$ multiplets can be attributed to phonon sidebands.

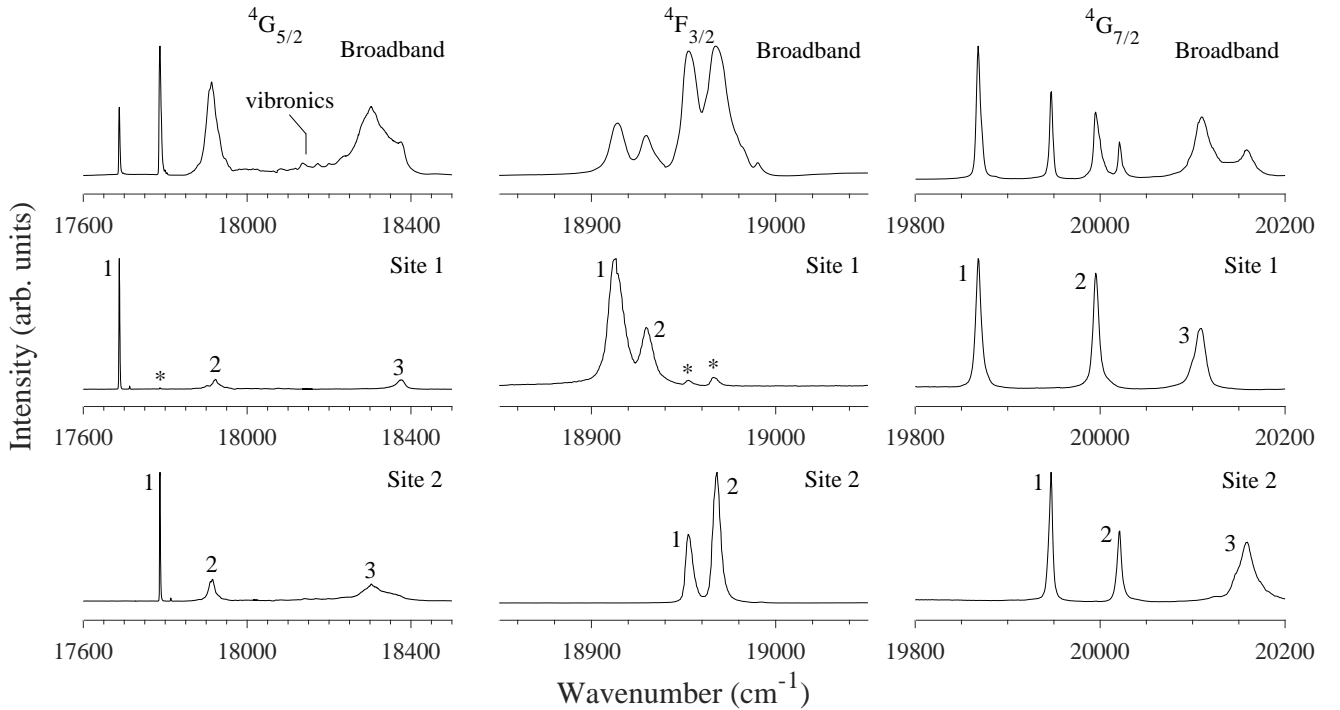


FIG. 2. 10 K broadband and site-selective excitation spectra of the ${}^4\text{G}_{5/2}$, ${}^4\text{F}_{3/2}$ and ${}^4\text{G}_{7/2}$ multiplets of both sites in $\text{Sm}^{3+}:\text{Y}_2\text{SiO}_5$. Numbered peaks are assignments to their respective site. Spectral features labelled with an ‘*’ are related to site 2. The additional structure observable in the spectra for the ${}^4\text{G}_{5/2}$ multiplet can be attributed to phonon sidebands.

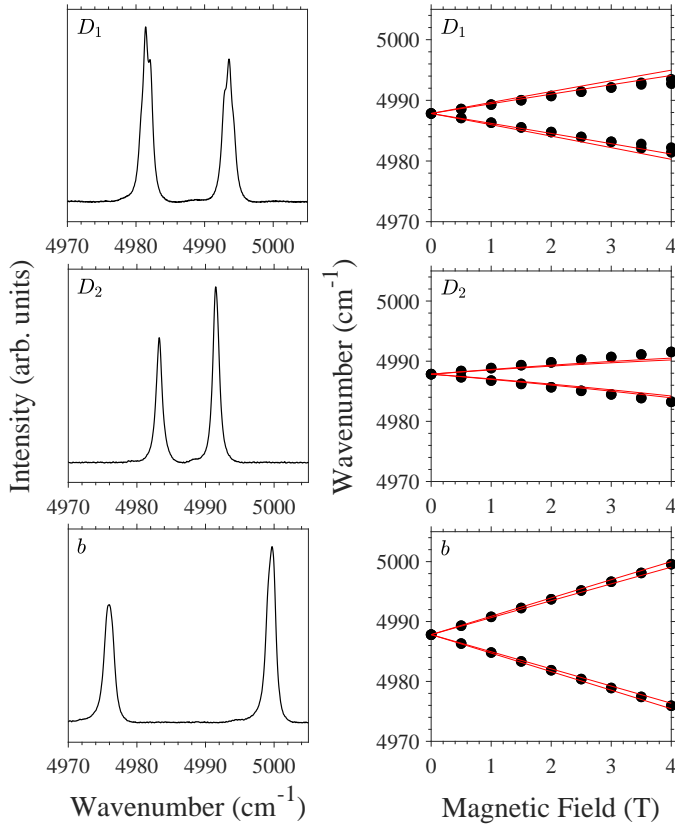


FIG. 3. Magnetic splittings of the ${}^6H_{5/2}Z_1 \rightarrow {}^6H_{13/2}V_1$ transition for site 1 in $\text{Sm}^{3+}:\text{Y}_2\text{SiO}_5$ with the magnetic field applied along the D_1 (top), D_2 (middle) and b (bottom) axes. The left panels show 4.2 K Zeeman absorption spectra at a magnetic field strength of 4 T. The right panels are the experimental splittings, shown by the circles, while the theoretical splittings are given as the red lines.

The contribution due to the electric quadrupole is given as:

$$H_Q = a_Q \frac{1}{2} \left(\frac{(I+1)(2I+1)(2I+3)}{I(2I-1)} \right)^{\frac{1}{2}} \mathbf{U}_n^{(2)} \cdot \mathbf{U}_e^{(2)} \quad (7)$$

where $\mathbf{U}_e^{(2)}$ and $\mathbf{U}_n^{(2)}$ are operators for the electronic and nuclear parts of the wave function respectively. The electric quadrupole hyperfine parameter, a_Q , is given as:

$$a_Q = \frac{-e^2 Q}{4\pi\epsilon_0} (1-R) \langle r_e^{-3} \rangle \quad (8)$$

here Q is the nuclear quadrupole moment. While a_l and a_Q can both be related to physical constants, they are typically determined from experimental data [22].

The final interaction given in Equation (1), the Zeeman interaction describes the effects of an external magnetic

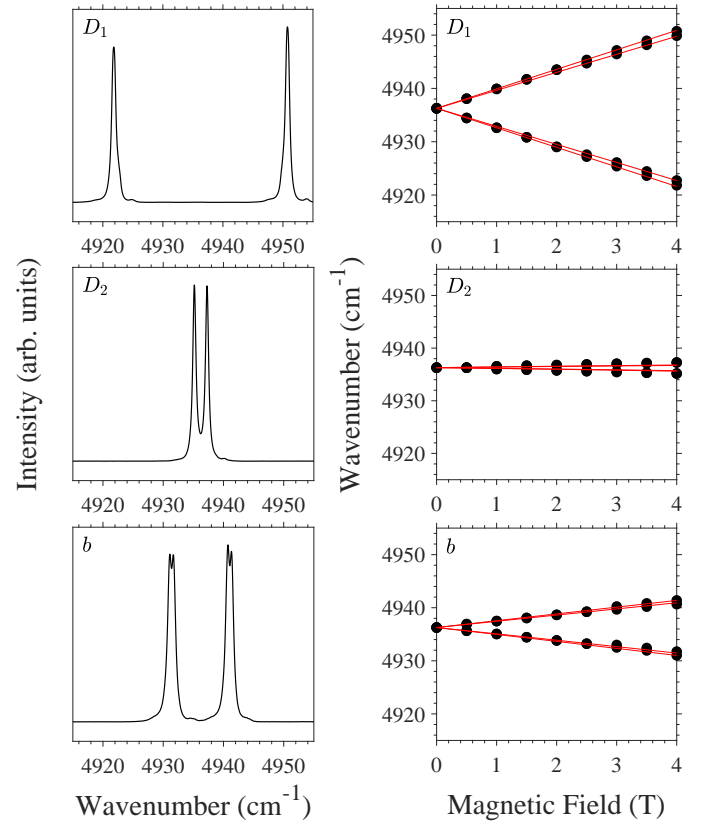


FIG. 4. Magnetic splittings of the ${}^6H_{5/2}Z_1 \rightarrow {}^6H_{13/2}V_1$ transition for site 2 in $\text{Sm}^{3+}:\text{Y}_2\text{SiO}_5$ with the magnetic field applied along the D_1 (top), D_2 (middle) and b (bottom) axes. The left panels show 4.2 K Zeeman absorption spectra at a magnetic field strength of 4 T. The right panels are the experimental splittings, shown by the circles, while the theoretical splittings are given as the red lines.

field, \mathbf{B} , and can be written as:

$$H_Z = \mu_B \sum_i^N \mathbf{B} \cdot (l_i + 2s_i) \quad (9)$$

where μ_B is the Bohr magneton, while l_i and s_i are the orbital and spin angular momenta of the i th electron respectively.

As noted above, in C_1 symmetry systems such as Y_2SiO_5 , there are 27 independent crystal-field parameters (counting real and imaginary parts as separate parameters), so crystal-field fits are very challenging. In the absence of directional interactions, such as applied magnetic fields, the energies are invariant under an arbitrary rotation, and so three of these parameters may be set to zero [38, 39]. Different rotations will lead to different parameters being zero and/or different magnitudes. Therefore, comparisons between parameters requires rotations to standardized parameter sets [40, 41].

In this work, magnetic splitting data is used to supply directional information. We use software developed by Horvath [21, 42, 43] to fit data for low-symmetry systems

using electronic energy levels, magnetic splittings, and hyperfine splittings (where available). A Monte-Carlo algorithm is used to search for the global minimum. We note that in a C_1 symmetry environment, measurements with magnetic fields along at least six different axes are required to fully determine the orientation. This is the number of measurements required to determine the g tensor for a Kramers doublet in C_1 symmetry.

The software developed by Horvath has been applied to extensive data sets for both sites of $\text{Er}^{3+}:\text{Y}_2\text{SiO}_5$. Initial work, which included g tensors for two states for each site, as well as hyperfine data [21] was later extended by using Zeeman spectroscopy to determine magnetic splittings along the D_1 , D_2 , and b axes of the crystal for dozens of states [42]. A similar approach has been independently applied to the two sites in $\text{Yb}^{3+}:\text{Y}_2\text{SiO}_5$ [23].

In the current work, we make use of electronic energy levels, g tensors determined for two electronic states [19], and magnetic splittings along the D_1 , D_2 , and b axes of the crystal for dozens of states. Hyperfine data is not yet available for $\text{Sm}^{3+}:\text{Y}_2\text{SiO}_5$.

The spin Hamiltonian for a Kramers doublet may be written as:

$$\mathcal{H} = \mu_B \mathbf{B} \cdot \mathbf{g} \cdot \mathbf{S} \quad (10)$$

where \mathbf{g} is the magnetic g tensor, while \mathbf{S} is the vector representation of the electronic spin operator. In our fits we use the experimental g tensors to calculate magnetic splittings at fields sampled from the following parametric spiral:

$$\mathbf{B} = B_0 \begin{bmatrix} \sqrt{1-t^2} \cos(6\pi t) \\ \sqrt{1-t^2} \sin(6\pi t) \\ t \end{bmatrix}, \quad t \in [-1, 1] \quad (11)$$

where B_0 is the magnitude of the magnetic field vector. Thus, for each site, we are fitting to magnetic splittings in many different directions for two states, in addition to the three axes (D_1 , D_2 , and b) for several dozen states. In order to reduce the required computational power, the matrix elements of the crystal-field levels were truncated to $30\,000\text{ cm}^{-1}$. The initial crystal-field parameters used in the optimization routine were those found for $\text{Er}^{3+}:\text{Y}_2\text{SiO}_5$ [21, 22]. All software used to perform the optimization is available from [43]. A coarse fit was performed using a basin hopping algorithm, which attempts a random step, followed by a local minimization which utilized the bound optimization by quadratic approximation (BOBYQA) algorithm [44–46]. The Metropolis criterion was applied to each random step, and if accepted, the algorithm was allowed to move to the newly found minima [47]. A final fit was then conducted using simulated annealing, which allows for the estimation of parameter uncertainties through the use of Markov-chain Monte-Carlo (MCMC) techniques [48].

For site 1 a total of 178 experimental data points were fitted simultaneously and are as follows:

- 56 electronic energy levels up to the ${}^4G_{7/2}$ multiplet at $\sim 20\,000\text{ cm}^{-1}$.
- 72 g values (25 along the D_1 axis, 22 along the D_2 axis and 25 along the b axis) corresponding to states up to the ${}^4G_{7/2}$ multiplet at $\sim 20\,000\text{ cm}^{-1}$.
- 25 data points for the magnetic splittings of the ${}^6H_{5/2}Z_1$ state, calculated from the g tensor given in [19], sampled at equally spaced intervals, with $B_0 = 0.05\text{ T}$.
- 25 data points for the magnetic splittings of the ${}^4G_{5/2}A_1$ state, calculated from the g tensor given in [19], sampled at equally spaced intervals according to Equation (11), with $B_0 = 0.05\text{ T}$.

For site 2 a total of 200 experimental data points were fitted simultaneously and are as follows:

- 58 electronic energy levels up to the ${}^4G_{7/2}$ multiplet at $\sim 20\,000\text{ cm}^{-1}$.
- 92 g values (34 along the D_1 axis, 28 along the D_2 axis and 30 along the b axis) corresponding to states up to the ${}^4G_{7/2}$ multiplet at $\sim 20\,000\text{ cm}^{-1}$.
- 25 data points for the magnetic splittings of the ${}^6H_{5/2}Z_1$ state, calculated from the g tensor given in [19], sampled at equally spaced intervals according to Equation (11), with $B_0 = 0.05\text{ T}$.
- 25 data points for the magnetic splittings of the ${}^4G_{5/2}A_1$ state, calculated from the g tensor given in [19], sampled at equally spaced intervals according to Equation (11), with $B_0 = 0.05\text{ T}$.

Tables I and II show the calculated and experimental electronic energy levels and g values up to the ${}^4G_{7/2}$ multiplet for site 1 and site 2 respectively in $\text{Sm}^{3+}:\text{Y}_2\text{SiO}_5$. The standard deviations between theoretical and experimental electronic energy levels were found to be 7.9 cm^{-1} for site 1 and 5.2 cm^{-1} for site 2. Furthermore, our study accurately reproduces the magnetic structure across a large portion of the entire $4f^5$ configuration of $\text{Sm}^{3+}:\text{Y}_2\text{SiO}_5$.

Table III shows the fitted free-ion and crystal-field parameters for both sites of $\text{Sm}^{3+}:\text{Y}_2\text{SiO}_5$, in the (D_1 , D_2 , b) frame. The two- and three-body interactions, in addition to the higher order effects given in Equation (2) were held fixed to the values found for $\text{Sm}^{3+}:\text{LaF}_3$ and are shown in Table IV [35]. Note that the two-fold symmetry of the crystal (not the sites) about the b axis gives rise to two magnetically inequivalent orientations for each site, which in general have different magnetic splittings unless the field is oriented along the b axis, or in the D_1 - D_2 plane. These parameter sets are related by a two-fold rotation, which gives a phase $e^{im\pi}$. This has the result of multiplying crystal-field parameters with odd q by -1 .

The parameter uncertainties were estimated through the use of MCMC techniques by sampling the posterior

TABLE I. Calculated and experimental electronic energies levels and g values up to $\sim 20\,000\text{ cm}^{-1}$ for site 1 in $\text{Sm}^{3+}:\text{Y}_2\text{SiO}_5$. All energies are in cm^{-1} . Levels marked with a ‘-’ were not observed.

Multiplet	State	Energies			g values						
		Calc.	Exp.	Diff.	D_1 axis		D_2 axis		b axis		
					Calc.	Exp.	Calc.	Exp.	Calc.	Exp.	
${}^6\text{H}_{5/2}$	Z ₁	-2	0	2	0.47	0.36	0.16	0.21	0.49	0.39	
	Z ₂	296	287	-9	1.30	-	0.36	-	1.04	-	
	Z ₃	505	486	-19	1.18	-	0.41	-	0.33	-	
${}^6\text{H}_{7/2}$	Y ₁	1156	1154	-2	0.88	-	1.00	-	4.09	-	
	Y ₂	1278	1275	-3	2.06	-	3.28	-	1.75	-	
	Y ₃	1480	1484	4	0.87	-	3.03	-	2.15	-	
	Y ₄	1550	1551	1	4.31	-	0.90	-	2.27	-	
${}^6\text{H}_{9/2}$	X ₁	2352	2351	-1	2.88	2.70	1.44	-	8.04	7.76	
	X ₂	2453	2461	8	5.09	-	3.37	-	3.41	-	
	X ₃	2539	2539	0	2.94	-	2.73	-	2.48	-	
	X ₄	2697	2702	5	1.74	-	6.34	-	3.79	-	
	X ₅	2761	2762	1	7.71	-	1.19	-	3.89	-	
${}^6\text{H}_{11/2}$	W ₁	3656	3661	5	4.69	4.50	1.26	2.34	11.41	11.58	
	W ₂	3723	3727	4	6.85	-	4.40	-	6.80	-	
	W ₃	3848	3841	-7	4.87	-	6.67	-	4.24	-	
	W ₄	3932	3934	2	4.54	-	3.72	-	5.12	-	
	W ₅	3997	3995	-2	5.45	-	8.18	-	5.84	-	
	W ₆	4067	4071	4	11.00	11.62	1.26	-	5.34	-	
${}^6\text{H}_{13/2}$	V ₁	4987	4988	1	7.41	6.05	3.36	4.44	12.68	12.65	
	V ₂	5035	5031	-4	7.16	5.27	4.13	5.74	10.51	11.27	
	V ₃	5244	5254	10	4.23	-	3.26	-	8.91	-	
	V ₄	5307	5312	5	5.09	-	7.36	-	4.68	-	
	V ₅	5364	5370	6	8.43	-	0.98	-	10.14	-	
	V ₆	5428	5423	-5	11.00	-	1.29	-	5.68	-	
	V ₇	5471	5469	-2	13.84	11.90	1.49	-	3.72	-	
${}^6\text{F}_{1/2}$,	S ₁	6198	6193	-5	9.02	7.15	4.24	6.67	13.48	13.96	
	${}^6\text{F}_{3/2}$,	S ₂	6394	6392	-2	6.66	-	3.62	-	12.12	-
${}^6\text{H}_{15/2}$	S ₃	6597	6583	-14	1.06	1.39	1.03	1.34	0.83	1.05	
	S ₄	6635	-	-	4.05	-	9.00	-	6.80	-	
	S ₅	6695	-	-	11.57	-	4.17	-	9.68	-	
	S ₆	6812	6823	9	3.61	-	4.15	-	3.90	-	
	S ₇	6839	-	-	2.36	-	3.10	-	2.99	-	
	S ₈	6862	6863	1	1.45	-	2.16	-	2.44	-	
	S ₉	6939	-	-	7.10	-	3.82	-	9.72	-	
	S ₁₀	7011	-	-	14.11	-	7.66	-	6.14	-	
	S ₁₁	7115	-	-	10.74	-	14.24	-	1.24	-	
	${}^6\text{F}_{5/2}$	R ₁	7335	7337	2	1.94	-	2.21	-	2.07	-
		R ₂	7385	7392	7	1.65	-	2.60	3.00	1.45	-
R ₃		7479	7472	-7	3.13	-	3.69	-	1.38	-	
${}^6\text{F}_{7/2}$	Q ₁	8167	8179	12	4.93	-	3.34	3.15	2.31	1.66	
	Q ₂	8195	8212	17	3.66	-	3.38	5.14	2.68	2.58	
	Q ₃	8246	8250	4	3.66	3.16	2.48	2.54	3.75	5.97	
	Q ₄	8363	8353	-10	4.28	4.59	4.28	5.06	4.03	3.85	
${}^6\text{F}_{9/2}$	P ₁	9315	9327	12	5.99	7.82	6.91	4.69	2.79	3.91	
	P ₂	9366	9372	6	4.44	6.06	4.50	4.82	4.51	4.19	
	P ₃	9400	9406	6	4.39	2.14	3.11	3.79	6.37	3.04	
	P ₄	9432	9445	13	3.36	3.17	1.17	2.07	7.33	8.48	
	P ₅	9495	9494	-1	4.81	4.12	3.61	4.82	8.17	8.46	
${}^6\text{F}_{11/2}$	O ₁	10650	10635	-15	11.90	13.17	1.30	-	6.95	6.46	
	O ₂	10683	10685	2	2.80	1.37	11.42	13.14	4.77	4.53	
	O ₃	10772	10777	5	5.80	7.81	6.33	5.52	5.03	3.90	
	O ₄	10837	10822	-15	6.54	8.49	7.80	9.28	2.90	2.04	
	O ₅	10862	10844	-18	7.66	6.17	7.77	5.83	2.68	7.31	
	O ₆	10927	10919	-8	1.62	3.05	0.65	-	14.79	14.84	
${}^4\text{G}_{5/2}$	A ₁	17690	17689	-1	1.19	1.07	1.09	1.29	2.43	2.46	
	A ₂	17920	17922	2	1.00	-	2.47	-	0.72	-	
	A ₃	18350	18355	5	1.95	-	1.15	-	1.74	-	
${}^4\text{F}_{3/2}$	B ₁	18912	18913	1	0.76	-	0.97	-	0.53	-	
	B ₂	18927	18929	2	0.94	-	0.45	-	0.73	-	
${}^4\text{G}_{7/2}$	C ₁	19866	19868	2	2.07	2.12	0.85	-	5.28	6.28	
	C ₂	20002	19995	-7	2.43	3.40	4.96	3.58	0.94	1.98	
	C ₃	20111	20109	-2	1.95	-	2.50	-	2.45	-	
	C ₄	20258	-	-	8.23	-	1.82	-	5.63	-	

TABLE II. Calculated and experimental electronic energies levels and g values up to $\sim 20\,000\text{ cm}^{-1}$ for site 2 in $\text{Sm}^{3+}:\text{Y}_2\text{SiO}_5$. All energies are in cm^{-1} . Levels marked with a ‘-’ were not observed.

Multiplet	State	Energies			g values						
		Calc.	Exp.	Diff.	D_1 axis		D_2 axis		b axis		
					Calc.	Exp.	Calc.	Exp.	Calc.	Exp.	
${}^6\text{H}_{5/2}$	Z ₁	1	0	-1	0.59	0.52	0.05	0.08	0.24	0.15	
	Z ₂	301	300	-1	0.69	-	0.95	-	0.44	-	
	Z ₃	438	429	-9	0.27	-	0.75	-	1.41	-	
${}^6\text{H}_{7/2}$	Y ₁	1121	1119	-2	4.78	-	1.18	-	0.91	-	
	Y ₂	1258	1256	-2	3.66	-	1.28	-	1.99	-	
	Y ₃	1419	1421	2	2.51	-	3.45	-	1.92	-	
	Y ₄	1465	1463	-2	1.27	-	2.48	-	3.23	-	
${}^6\text{H}_{9/2}$	X ₁	2317	2322	5	8.41	7.92	1.95	1.48	1.15	1.63	
	X ₂	2412	2415	3	6.74	6.15	1.12	-	3.66	4.32	
	X ₃	2558	2564	6	4.12	-	3.69	-	2.10	-	
	X ₄	2626	2627	1	3.28	-	5.46	-	5.41	6.49	
	X ₅	2661	2660	-1	2.54	-	4.39	6.07	4.40	-	
${}^6\text{H}_{11/2}$	W ₁	3610	3615	5	11.92	11.93	1.41	0.69	2.75	2.56	
	W ₂	3708	3713	5	9.97	10.10	1.11	-	3.52	4.00	
	W ₃	3837	3833	-4	7.25	7.06	3.34	-	3.14	-	
	W ₄	3904	3906	2	2.85	3.90	6.33	4.10	2.93	-	
	W ₅	3937	3940	3	5.99	-	2.60	-	7.83	-	
	W ₆	3985	3987	2	1.59	-	5.35	8.02	8.75	7.99	
${}^6\text{H}_{13/2}$	V ₁	4935	4936	1	15.09	15.01	0.58	1.12	5.31	5.17	
	V ₂	5125	5124	-1	13.44	13.89	2.83	-	2.85	-	
	V ₃	5201	5199	-2	8.84	9.01	5.89	6.97	4.58	3.17	
	V ₄	5242	5244	2	4.14	3.12	8.36	10.04	4.20	-	
	V ₅	5304	5301	-3	5.80	5.68	7.41	-	4.75	-	
	V ₆	5342	5337	-5	2.99	8.23	7.05	7.23	9.76	-	
	V ₇	5409	5414	5	2.60	-	6.39	8.76	13.90	12.35	
${}^6\text{F}_{1/2}$,	S ₁	6218	6217	-1	17.87	17.86	1.24	0.95	6.30	6.70	
${}^6\text{F}_{3/2}$,	S ₂	6528	6514	-14	1.07	-	1.92	0.99	1.44	1.68	
${}^6\text{H}_{15/2}$	S ₃	6546	-	-	10.15	-	4.66	-	3.78	-	
	S ₄	6582	-	-	5.01	-	10.48	-	2.97	-	
	S ₅	6665	-	-	5.84	-	6.97	-	6.19	-	
	S ₆	6748	6752	4	1.67	-	3.76	-	6.43	-	
	S ₇	6772	-	-	2.36	-	3.10	-	2.93	-	
	S ₈	6798	6792	-6	1.65	-	2.09	-	1.15	-	
	S ₉	6838	6832	-6	2.63	-	4.09	-	10.64	-	
	S ₁₀	6875	6873	-2	10.99	-	10.40	-	4.16	-	
	S ₁₁	6917	6912	-5	3.78	-	3.81	-	14.38	-	
	${}^6\text{F}_{5/2}$	R ₁	7280	7281	1	4.14	3.75	2.72	-	0.55	2.54
		R ₂	7303	7308	5	2.28	3.27	0.69	-	2.94	2.38
R ₃		7356	7350	-6	2.64	-	2.98	-	2.56	-	
${}^6\text{F}_{7/2}$	Q ₁	8107	8117	10	2.93	2.26	4.01	1.55	3.00	2.50	
	Q ₂	8143	8152	9	2.46	2.67	4.82	3.44	3.44	4.29	
	Q ₃	8185	8184	-1	6.91	7.16	2.17	1.88	2.34	2.42	
	Q ₄	8216	8214	-2	1.67	-	5.58	4.64	4.08	5.61	
${}^6\text{F}_{9/2}$	P ₁	9269	9270	1	5.35	2.80	4.07	6.40	7.83	7.24	
	P ₂	9297	9300	3	6.29	3.39	1.85	1.86	4.80	6.03	
	P ₃	9324	9337	13	4.78	3.38	7.32	5.32	2.76	2.59	
	P ₄	9346	9354	8	4.25	8.55	6.04	-	3.31	2.79	
	P ₅	9405	9408	3	10.33	11.18	1.86	-	3.22	-	
${}^6\text{F}_{11/2}$	O ₁	10623	10612	-11	4.05	4.83	6.20	6.57	10.97	11.93	
	O ₂	10645	10635	-10	4.02	2.69	2.94	2.70	6.59	8.66	
	O ₃	10683	10675	-8	6.06	5.72	4.01	4.40	3.10	4.32	
	O ₄	10729	10726	-3	9.49	9.35	2.42	2.48	4.53	4.39	
	O ₅	10774	10783	9	11.47	10.07	6.15	-	7.90	-	
	O ₆	10820	10817	-3	13.25	14.24	8.49	-	0.83	-	
${}^4\text{G}_{5/2}$	A ₁	17795	17790	-5	2.97	3.29	0.37	0.38	0.78	0.77	
	A ₂	17922	17915	-7	2.31	-	0.59	-	1.01	-	
	A ₃	18282	18291	9	1.15	-	2.18	-	1.69	-	
${}^4\text{F}_{3/2}$	B ₁	18953	18955	2	0.33	0.79	1.17	0.75	0.69	-	
	B ₂	18971	18968	-3	0.88	-	0.39	0.91	0.99	0.79	
${}^4\text{G}_{7/2}$	C ₁	19947	19947	0	6.16	6.99	2.25	1.21	0.82	1.07	
	C ₂	20016	20021	5	3.99	4.75	2.06	-	2.80	2.25	
	C ₃	20159	20159	0	3.72	-	1.43	-	0.74	-	
	C ₄	20296	-	-	1.38	-	4.02	-	3.51	-	

probability distribution. A total of 5 000 000 trials were attempted for both sites with 423 818 accepted steps for site 1 and 401 830 accepted steps for site 2. This aligns with the Metropolis algorithms $\sim 10\%$ acceptance rate recommended for this technique, which was fine tuned through altering the step size in the optimization routine [48]. The algorithm was allowed to ‘burn in’ (become confined within the area of the global minimum), and every 10^{th} element of the remaining 50 000 steps were then selected to ensure that the samples were not correlated. Our Monte-Carlo approach is designed to locate the global minimum, and trials with different starting parameters lead to similar fitted parameters.

Table V shows the g tensors determined from our crystal-field analysis for the ${}^6\text{H}_{5/2}\text{Z}_1$ and ${}^4\text{G}_{5/2}\text{A}_1$ states for both sites in $\text{Sm}^{3+}:\text{Y}_2\text{SiO}_5$. The experimental g tensors are also given for comparison [19]. It can be seen that the calculation gives good account of the experimental data.

Table VI shows the predicted zero-field hyperfine splittings of the ${}^6\text{H}_{5/2}\text{Z}_1$ ground and ${}^4\text{G}_{5/2}\text{A}_1$ excited states for both sites in $\text{Sm}^{3+}:\text{Y}_2\text{SiO}_5$. As the hyperfine parameters are largely host invariant, the hyperfine parameter determined for $\text{Sm}^{3+}:\text{CaF}_2$, co-doped with Na^{3+} ions, was used in our predictions [49]. It should be noted that the nuclear-quadrupole parameter was not determined in [49] and was set to zero in our predictions. The ground state (${}^6\text{H}_{5/2}\text{Z}_1$) hyperfine structure is predicted to span about 4 GHz for both sites, while the excited state (${}^4\text{G}_{5/2}\text{A}_1$) of both sites is expected to span about 2.5 GHz. These are splittings on the same order as that of $\text{Er}^{3+}:\text{Y}_2\text{SiO}_5$, and are much larger than the hyperfine splittings of $\text{Eu}^{3+}:\text{Y}_2\text{SiO}_5$. As such we believe $\text{Sm}^{3+}:\text{Y}_2\text{SiO}_5$ could be an attractive candidate for high-bandwidth quantum memories [14, 21].

Crystal-field parameters in higher-symmetry sites show a reasonably consistent trend across the rare-earth series (see, for example [35]). For Y_2SiO_5 the only published fits that make use of directional magnetic data are for Er^{3+} [21, 42], Yb^{3+} [23], and this work. In comparing parameter sets for different ions, we must take into account that for each site there are two magnetically-inequivalent orientations, which are related by changing the sign of the odd- q crystal-field parameters. We note

that for Yb^{3+} there are only a small number of electronic levels and for Sm^{3+} , the hyperfine splittings are not available. The parameters obtained here are broadly similar to the parameters for Er^{3+} , but it is an open question how much they would change with additional data in the fit.

IV. CONCLUSIONS

We have presented parameterized crystal-field analyses for both the six and seven fold coordinated C_1 point group symmetry substitutional sites of $\text{Sm}^{3+}:\text{Y}_2\text{SiO}_5$, based upon a large quantity of detailed laser spectroscopy and Zeeman measurements. Approximately fifty-five electronic energy levels, up to the ${}^4\text{G}_{7/2}$ multiplet at $\sim 20\,000\text{ cm}^{-1}$ and eighty g values, obtained along all three crystallographic axes, in addition to magnetic splittings determined from the previously determined g tensors of the ${}^6\text{H}_{5/2}\text{Z}_1$ and ${}^4\text{G}_{5/2}\text{A}_1$ states [19], were fitted simultaneously for each site in order to obtain an unambiguous fit. Good agreement is obtained between the calculation and experimental data over the entire portion of the $4f^5$ configuration for which we could make measurements.

We have also predicted the zero-field hyperfine structure for both sites of $\text{Sm}^{3+}:\text{Y}_2\text{SiO}_5$. The hyperfine splittings are estimated to be of a similar magnitude to those previously reported for $\text{Er}^{3+}:\text{Y}_2\text{SiO}_5$ [21]. This, coupled with the small magnetic splittings of the Sm^{3+} ground state suggest that this material could be a previously unexplored alternative in the development of high-bandwidth quantum information storage and communications devices.

ACKNOWLEDGMENTS

N.L.J. would like to thank the Dodd-Walls Centre for Photonic and Quantum Technologies for the provision of a PhD studentship. The technical assistance of Mr. S. Hemmingson, Mr. R. J. Thirkettle and Mr. G. MacDonald is gratefully acknowledged.

-
- [1] J. Wesenberg and K. Mølmer, Robust quantum gates and a bus architecture for quantum computing with rare-earth-ion-doped crystals, *Phys. Rev. A* **68**, 012320 (2003).
 - [2] E. Fraval, M. J. Sellars, A. Morrison, and A. Ferris, Pr–Y interaction in $\text{Pr}^{3+}:\text{Y}_2\text{SiO}_5$, *J. Lumin.* **107**, 347 (2004).
 - [3] G. Heinze, C. Hubrich, and T. Halfmann, Stopped light and image storage by electromagnetically induced transparency up to the regime of one minute, *Phys. Rev. Lett.* **111**, 033601 (2013).
 - [4] M. Zhong, M. P. Hedges, R. L. Ahlefeldt, J. G. Bartholomew, S. E. Beavan, S. M. Wittig, J. J. Longdell, and M. J. Sellars, Optically addressable nuclear spins in a solid with a six-hour coherence time, *Nature* **517**, 177 (2015).
 - [5] H. de Riedmatten, M. Afzelius, M. U. Staudt, C. Simon, and N. Gisin, A solid-state light-matter interface at the single-photon level, *Nature* **456**, 773 (2008).
 - [6] T. Zhong, J. M. Kindem, J. G. Bartholomew, J. Rochman, I. Craiciu, E. Miyazono, M. Bettinelli, E. Cavalli, V. Verma, S. W. Nam, F. Marsili, M. D. Shaw, A. D. Beyer, and A. Faraon, Nanophotonic rare-earth

TABLE III. Fitted values for the free-ion and crystal-field parameters and their related uncertainties of site 1 and site 2 in $\text{Sm}^{3+}:\text{Y}_2\text{SiO}_5$. All values are in cm^{-1} . Note that the two magnetically inequivalent orientations for each site, are related by a two-fold rotation about the b axis. This has the result of multiplying crystal-field parameters with odd q by -1 .

Parameter	Site 1		Site 2	
	Site 1	Site 1 Uncertainty	Site 2	Site 2 Uncertainty
E_{avg}	47316	1	47338	1
F^2	78297	3	78391	3
F^4	56463	5	56606	5
F^6	39727	4	39876	6
ζ	1165.98	1	1169	1
B_0^2	-511	5	446	9
B_1^2	$603 + 241i$	$6 + 5i$	$329 - 104i$	$8 + 8i$
B_2^2	$91 - 62i$	$5 + 4i$	$-460 - 62i$	$7 + 8i$
B_0^4	2068	7	810	8
B_1^4	$167 + 507i$	$5 + 13i$	$-539 + 40i$	$10 + 8i$
B_2^4	$-144 + 466i$	$6 + 7i$	$-85 - 605i$	$8 + 11i$
B_3^4	$-299 - 112i$	$4 + 2i$	$-181 + 440i$	$9 + 10i$
B_4^4	$-901 + 1021i$	$6 + 3i$	$-994 + 80i$	$10 + 9i$
B_0^6	-45	5	521	9
B_1^6	$534 - 52i$	$3 + 8i$	$-241 - 68i$	$11 + 5i$
B_2^6	$109 + 271i$	$4 + 2i$	$-324 + 161i$	$12 + 9i$
B_3^6	$266 + 84i$	$5 + 6i$	$-54 + 22i$	$7 + 7i$
B_4^6	$371 - 199i$	$6 + 5i$	$-17 + 44i$	$8 + 10i$
B_5^6	$-155 - 27i$	$12 + 8i$	$38 + 20i$	$8 + 14i$
B_6^6	$-81 - 46i$	$5 + 7i$	$423 + 253i$	$6 + 7i$

TABLE IV. Parameters that were held fixed during the fitting process and were set to those found by Carnall *et al.* in $\text{Sm}^{3+}:\text{LaF}_3$ [35].

Parameter	Value
α	20.16
β	-566.9
γ	1500
T^2	300
T^3	36
T^4	56
T^6	-347
T^7	373
T^8	348
M^0	2.6
P^2	357

quantum memory with optically controlled retrieval, Science **357**, 1392 (2017).

- [7] M. Rančić, M. P. Hedges, R. L. Ahlefeldt, and M. J. Sellars, Coherence time of over a second in a telecom-compatible quantum memory storage material, Nat. Phys **14**, 50–54 (2018).
- [8] J. J. Longdell and M. J. Sellars, Experimental demonstration of quantum-state tomography and qubit-qubit interactions for rare-earth-metal-ion-based solid-state qubits, Phys. Rev. A **69**, 032307 (2004).
- [9] L. Rippe, B. Julsgaard, A. Walther, Y. Ying, and S. Kröll, Experimental quantum-state tomography of a solid-state qubit, Phys. Rev. A **77**, 022307 (2008).
- [10] A. M. Dibos, M. Raha, C. M. Phenicie, and J. D. Thomp-

son, Atomic source of single photons in the telecom band, Phys. Rev. Lett. **120**, 243601 (2018).

- [11] S. Chen, M. Raha, C. M. Phenicie, S. Ourari, and J. D. Thompson, Parallel single-shot measurement and coherent control of solid-state spins below the diffraction limit, Science **370**, 592 (2020).
- [12] J. J. Longdell, M. J. Sellars, and N. B. Manson, Hyperfine interaction in ground and excited states of praseodymium-doped yttrium orthosilicate, Phys. Rev. B **66**, 035101 (2002).
- [13] M. Lovrić, P. Glasenapp, and D. Suter, Spin hamiltonian characterization and refinement for $\text{Pr}^{3+}:\text{YAlO}_3$ and $\text{Pr}^{3+}:\text{Y}_2\text{SiO}_5$, Phys. Rev. B **85**, 014429 (2012).
- [14] J. J. Longdell, A. L. Alexander, and M. J. Sellars, Characterization of the hyperfine interaction in europium-doped yttrium orthosilicate and europium chloride hexahydrate, Phys. Rev. B **74**, 195101 (2006).
- [15] A. Ortu, A. Tiranov, S. Welinski, F. Fröwis, N. Gisin, A. Ferrier, P. Goldner, and M. Afzelius, Simultaneous coherence enhancement of optical and microwave transitions in solid-state electronic spins, Nat. Mater **17**, 671 (2018).
- [16] J. V. Rakonjac, Y.-H. Chen, S. P. Horvath, and J. J. Longdell, Long spin coherence times in the ground state and in an optically excited state of $^{167}\text{Er}^{3+}:\text{Y}_2\text{SiO}_5$ at zero magnetic field, Phys. Rev. B **101**, 184430 (2020).
- [17] S. Welinski, A. Ferrier, M. Afzelius, and P. Goldner, High-resolution optical spectroscopy and magnetic properties of Yb^{3+} in Y_2SiO_5 , Phys. Rev. B **94**, 155116 (2016).
- [18] O. Guillot-Noël, P. Goldner, Y. L. Du, E. Baldit, P. Monnier, and K. Bencheikh, Hyperfine interaction of Er^{3+} ions in Y_2SiO_5 : An electron paramagnetic resonance

TABLE V. Calculated and experimental [19] g tensors for the ${}^6\text{H}_{5/2}\text{Z}_1$ and ${}^4\text{G}_{5/2}\text{A}_1$ states for both sites in $\text{Sm}^{3+}:\text{Y}_2\text{SiO}_5$.

State	Site 1						Site 2						
	g_{xx}	g_{yy}	g_{zz}	g_{xy}	g_{xz}	g_{yz}	g_{xx}	g_{yy}	g_{zz}	g_{xy}	g_{xz}	g_{yz}	
${}^6\text{H}_{5/2}\text{Z}_1$	Calc.	0.448	0.084	0.487	-0.120	0.044	0.068	0.574	0.047	0.186	0.010	-0.147	-0.009
	Expt.	0.351	0.209	0.382	-0.016	0.078	-0.007	0.512	0.067	0.135	-0.040	-0.054	0.009
${}^4\text{G}_{5/2}\text{A}_1$	Calc.	1.113	0.979	2.405	-0.373	-0.203	0.265	2.932	0.260	0.531	0.184	-0.526	-0.112
	Expt.	1.025	1.248	2.446	-0.257	0.166	0.202	3.264	0.183	0.714	-0.311	0.262	0.125

TABLE VI. Calculated zero-field hyperfine splittings of the ${}^6\text{H}_{5/2}\text{Z}_1$ and ${}^4\text{G}_{5/2}\text{A}_1$ states for both sites in $\text{Sm}^{3+}:\text{Y}_2\text{SiO}_5$. Level 1 is defined as the zero point for both states. All values are in GHz.

Level	Site 1		Site 2	
	${}^6\text{H}_{5/2}\text{Z}_1$	${}^4\text{G}_{5/2}\text{A}_1$	${}^6\text{H}_{5/2}\text{Z}_1$	${}^4\text{G}_{5/2}\text{A}_1$
1	0	0	0	0
2	0	0.00009	0	0
3	0.54397	0.19639	0.62839	0.37123
4	0.54418	0.20260	0.62839	0.37123
5	1.05596	0.32120	1.25634	0.73821
6	1.07575	0.38388	1.25640	0.73959
7	1.40441	0.41584	1.85338	1.05146
8	1.93090	1.64454	1.91618	1.15621
9	2.12520	1.65656	2.46357	1.36463
10	2.52932	1.82643	2.56955	1.65387
11	2.88649	1.90452	3.14710	1.90710
12	2.90277	1.94182	3.14722	1.91052
13	3.42318	2.11417	3.77467	2.26925
14	3.42336	2.11635	3.77467	2.26925
15	3.96940	2.34102	4.40302	2.63865
16	3.96940	2.34105	4.40302	2.63865

spectroscopy study, Phys. Rev. B **74**, 214409 (2006).

- [19] N. L. Jobbitt, J.-P. R. Wells, M. F. Reid, and J. J. Longdell, Raman heterodyne determination of the magnetic anisotropy for the ground and optically excited states of Y_2SiO_5 doped with Sm^{3+} , Phys. Rev. B **103**, 205114 (2021).
- [20] Y. Alizadeh, J. L. B. Martin, M. F. Reid, and J.-P. R. Wells, Intra- and inter-configurational electronic transitions of Ce^{3+} -doped Y_2SiO_5 : Spectroscopy and crystal field analysis, Opt. Mater. **117**, 111114 (2021).
- [21] S. P. Horvath, J. V. Rakonjac, Y.-H. Chen, J. J. Longdell, P. Goldner, J.-P. R. Wells, and M. F. Reid, Extending phenomenological crystal-field methods to C_1 point-group symmetry: Characterization of the optically excited hyperfine structure of ${}^{167}\text{Er}^{3+}:\text{Y}_2\text{SiO}_5$, Phys. Rev. Lett. **123**, 057401 (2019).
- [22] S. P. Horvath, *High-resolution spectroscopy and novel crystal-field methods for rare-earth based quantum information processing*, Ph.D. thesis, University of Canterbury (2016).
- [23] X. Zhou, H. Liu, Z. He, B. Chen, and J. Wu, Investigation of the electronic structure and optical, epr, and odmr spectroscopic properties for ${}^{171}\text{Yb}^{3+}$ -doped Y_2SiO_5 crystal: A combined theoretical approach, Inorg. Chem. **59**, 13144 (2020), pMID: 32865403.
- [24] N. L. Jobbitt, S. J. Patchett, Y. Alizadeh, M. F. Reid, J.-P. R. Wells, S. P. Horvath, J. J. Longdell, A. Ferrier, and P. Goldner, Transferability of crystal-field parameters for rare-earth ions in Y_2SiO_5 tested by Zeeman spectroscopy, Phys. Sol. State **61**, 780 (2019).
- [25] S. Mothkuri, M. F. Reid, J.-P. R. Wells, E. Lafitte-Houssat, P. Goldner, and A. Ferrier, Electron-nuclear interactions as a test of crystal field parameters for low-symmetry systems: Zeeman hyperfine spectroscopy of Ho^{3+} -doped Y_2SiO_5 , Phys. Rev. B **103**, 104109 (2021).
- [26] B. A. Maksimov, V. V. Ilyukhin, Y. A. Kharitonov, and N. V. Belov, Crystal structure of yttrium oxyorthosilicate $\text{Y}_2\text{O}_3 \cdot \text{SiO}_2 = \text{Y}_2\text{SiO}_5$, Kristallografiya **15**, 926 (1970).
- [27] C. Li, C. Wyon, and R. Moncorge, Spectroscopic properties and fluorescence dynamics of $\text{Er}^{3+}:\text{Y}_2\text{SiO}_5$, IEEE J. Quantum Electron. **28**, 1209 (1992).
- [28] Y. Sun, T. Böttger, C. Thiel, and R. Cone, Magnetic g tensors for the ${}^4\text{I}_{15/2}$ and ${}^4\text{I}_{13/2}$ states of $\text{Er}^{3+}:\text{Y}_2\text{SiO}_5$, Phys. Rev. B **77**, 085124 (2008).
- [29] N. L. Jobbitt, J.-P. R. Wells, and M. F. Reid, Energy transfer between Sm^{3+} ions in Y_2SiO_5 crystals, J. Lumin. **224**, 117302 (2020).
- [30] J.-P. R. Wells, M. Yamaga, T. P. J. Han, H. G. Gallagher, and M. Honda, Polarized laser excitation, electron paramagnetic resonance and crystal-field analyses of Sm^{3+} -doped LiYF_4 , Phys. Rev. B. **60**, 3849 (1999).
- [31] J.-P. R. Wells and R. J. Reeves, Polarized laser-selective excitation and Zeeman infrared absorption of Sm^{3+} centres in CaF_2 and SrF_2 crystals, Phys. Rev. B. **61**, 13593 (2000).
- [32] J.-P. R. Wells, A. Sugiyama, T. P. J. Han, and H. G. Gallagher, Laser site selective excitation of KY_3F_{10} doped with samarium, J. Lumin. **85**, 91 (1999).
- [33] Y. Luo, L. Sun, J. Wang, Z. Tian, H. Nian, and J. Wang, Tunable thermal properties in yttrium silicates switched by anharmonicity of low-frequency phonons, J. Eur. Ceram. Soc. **38**, 2043 (2018).
- [34] G. Liu, *Spectroscopic properties of rare earths in optical materials*, edited by G. Liu and B. Jacquier (Springer Science & Business Media, 2006).
- [35] W. T. Carnall, G. L. Goodman, K. Rajnak, and R. S. Rana, A systematic analysis of the spectra of the lanthanides doped into single crystal LaF_3 , J. Chem. Phys. **90**, 3443 (1989).
- [36] B. R. Judd, *Operator Techniques in Atomic Spectroscopy* (Princeton University Press, 1998).
- [37] B. G. Wybourne, *Spectroscopic Properties of Rare Earths* (Interscience Publishers, 1965).
- [38] P. Gnutek and C. Rudowicz, Diagonalization of second-rank crystal field terms for $3d^N$ and $4f^N$ ions at triclinic or monoclinic symmetry sites – case study: Cr^{4+} in $\text{Li}_2\text{MgSiO}_4$ and Nd^{3+} in $\beta\text{-BaB}_2\text{O}_4$, Optical Materials **31**, 391 (2008).

- [39] G. W. Burdick and M. F. Reid, Crystal field parametrizations for low symmetry systems, *Molecular Physics* **102**, 1141 (2004).
- [40] C. Rudowicz and R. Bramley, On standardization of the spin Hamiltonian and the ligand field Hamiltonian for orthorhombic symmetry, *The Journal of Chemical Physics* **83**, 5192 (1985).
- [41] C. Rudowicz, D. Yadav, R. Kripal, and P. Gnutek, Standardization of crystal field parameters for rare-earth (RE^{3+}) ions at monoclinic sites in selected laser crystals, *Journal of Alloys and Compounds* **666**, 468 (2016).
- [42] N. L. Jobbitt, J.-P. R. Wells, M. F. Reid, S. P. Horvath, P. Goldner, and A. Ferrier, Prediction of optical polarization and high-field hyperfine structure via a parametrized crystal-field model for low-symmetry centers in Er^{3+} -doped Y_2SiO_5 , *Phys. Rev. B* **104**, 155121 (2021).
- [43] S. Horvath, The pycf crystal-field theory package, <https://bitbucket.org/sebastianhorvath/pycf>.
- [44] D. J. Wales and J. P. K. Doye, Global optimization by basin-hopping and the lowest energy structures of Lennard-Jones clusters containing up to 110 atoms, *J. Phys. Chem. A* **101**, 5111 (1997).
- [45] D. J. Wales and H. A. Scheraga, Global optimization of clusters, crystals, and biomolecules, *Science* **285**, 1368 (1999).
- [46] S. G. Johnson, The nlopt nonlinear-optimization package, <http://ab-initio.mit.edu/nlopt>.
- [47] N. Metropolis, A. W. Rosenbluth, M. N. Rosenbluth, A. H. Teller, and E. Teller, Equation of state calculations by fast computing machines, *J. Chem. Phys* **21**, 1087 (1953).
- [48] R. C. Aster, B. Borchers, and C. H. Thurber, *Parameter estimation and inverse problems*, Vol. 90 (Academic Press, 2011).
- [49] S. P. Horvath, J.-P. R. Wells, M. F. Reid, M. Yamaga, and M. Honda, Electron paramagnetic resonance enhanced crystal field analysis for low point-group symmetry systems: C_{2v} sites in $\text{Sm}^{3+}:\text{CaF}_2/\text{SrF}_2$, *J. Phys. Condens. Matter* **31**, 015501 (2018).